ChemComm

Accepted Manuscript

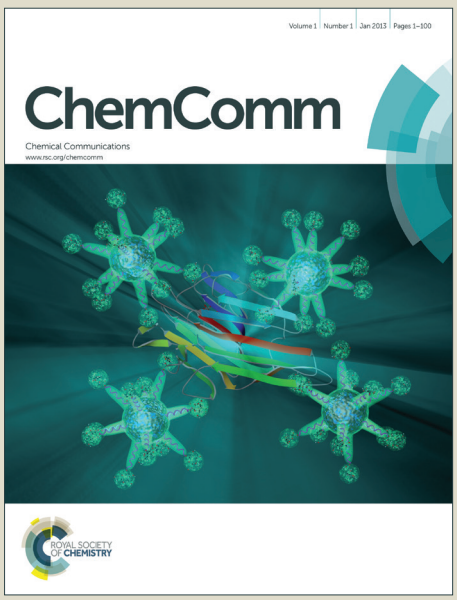

ROYAL SOCIETY OF CHEMISTRY

www.rsc.org/chemcomm

Journal Name

RSCPublishing

COMMUNICATION

High interfacial lithium storage capability of hollow porous Mn_2O_3 nanostructures obtained from carbonate precursors

Cite this: DOI: 10.1039/xoxxoooooox

Received ooth January 2012,
Accepted ooth January 2012

DOI: 10.1039/xoxxoooooox

www.rsc.org/

Rui Liu, Shiqiang Zhao, Miaomiao Zhang, Fan Feng and Qiang Shen*

Preparation of porous Mn_2O_3 boxes has been developed via a carbonate precursor route. As a Li-ion battery anode, it delivers a high reversible capacity of 1442 mA h g^{-1} over 600 cycles at 800 mA g^{-1}, and 65% the capacity originates from the gradually emerging interfacial storage contribution.

Mn_2O_3 has been regarded as an appealing anode material for Li-ion batteries (LIBs) owing to its high theoretical capacity, low operating voltage, earth-abundance, nontoxicity and low processing cost.[1-3] In principle, the conversion reaction of a transition metal oxide (TMO) with metallic Li results in highly dispersed transition metal nanoparticles and electrochemically inactive Li_2O matrix, and the enhanced surface energy favors the Li_2O reversibility catalyzed by metallic nanocrystals.[4] This deals with a large volume change or a high capacity loss and even destroys the integrity of assembled electrode upon discharge-charge cycling, especially at a high current rate.[5] Aside from the bulk insertion of Li^+ ions, both the faradaic contribution of pseudocapacitance and nonfaradaic contribution of double-layer capacitance are reasonably referred to as an interfacial storage capability to offset the capacity loss.[6, 7] In most cases the interfacial storage capacity of bare TMOs can outstand when the active nanoparticles are highly dispersed and effectively stabilized by a nanostructured matrix such as carbonaceous materials.[3, 8-11]

Constructing the hollow porous nanostructures of TMO with a high specific surface area is a promising approach to improve its Li storage capacity.[12] This structural feature facilitates the close contact of active substance with electrolyte, reduces the diffusion path of Li ions and favors the conversion reaction of the TMO with metallic Li. Moreover, both the porous shells and hollow interiors can effectively buffer the volume change of a working electrode occurring during the reversible processes of Li-ion insertion/extraction. To date, the hollow porous nanostructures of Co_3O_4, SnO_2, Fe_3O_4 and $LiMn_2O_4$ have been prepared successfully, however, as LIB anodes only the acquired electrochemical properties of high reversible capacity, good cycling stability and/or rate capability, not the non-faradaic contribution, have been highlighted therein.[13-16] Therefore, it is of crucial importance to evidence the possible relationship between the high interfacial Li storage capability and the high specific surface area of nanostructured TMOs with a hollow porous feature.

Several experimental efforts have been carried out for the controlling synthesis and potential applicability of Mn_2O_3 applied as LIB anodes, and unfortunately its non-faradaic contribution of specific surface area to the improved lithium storage capability is still difficult to be demonstrated visually.[2, 17-19] Herein, the slow ion-exchange reaction of solid-state vaterite (i.e., the instable polymorph of anhydrous $CaCO_3$) with aqueous $MnCl_2$ was firstly adopted to prepare cube-shaped $MnCO_3$,[20, 21] not the loose aggregates of tiny nanoparticles in case of the structural collapse occurring during the direct transformation of $MnCO_3$ into oxides. Secondly, a well-known $KMnO_4$-assisted wet-chemical oxidation of precursor $MnCO_3$ was used to produce amorphous MnO_2 boxes.[22] And then, a high-temperature calcination of intermediate MnO_2 guarantees the final generation of porous Mn_2O_3 boxes, defined as Mn_2O_3-1 sample. When evaluated as a LIB anode, the reversible capacity of Mn_2O_3-1 electrode initially expresses a routine downward trend owing to gradual capacity loss and thereafter exhibits an upward trend owing to the gradually outstood interfacial storage, reaching a high value of 712 mA h g^{-1} over 600 cycles at 1600 mA g^{-1}.

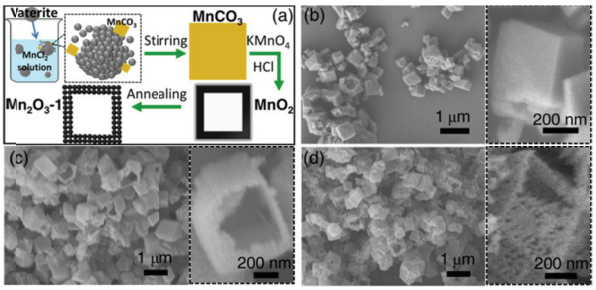

Fig. 1 (a) A schematic drawing of porous Mn_2O_3 boxes obtained from carbonate precursors. (b-d) SEM images of precursor $MnCO_3$, intermediate MnO_2 boxes and finally produced porous Mn_2O_3 boxes in sequence.

Fig. 1a schematically illustrates a three-step procedure to obtain porous Mn_2O_3 boxes. The first step deals with an ion-exchange reaction from crystalline $CaCO_3$ to $MnCO_3$ driven by their different solubility products, which is slow and at least six hours are needed to obtain $MnCO_3$ cubes (Fig. S1, S2†). In the second step, at the

$KMnO_4$:$MnCO_3$ molar ratio of 1:30 the resulting MnO_2 boxes are directly rinsed using HCl aqueous solution (1.2 M) to remove unreacted $MnCO_3$ within the cubes' interior (Fig. 1a). By increasing the molar ratio of $KMnO_4$ to $MnCO_3$ to 1:1.5, porous Mn_2O_3 boxes with a smaller interior can be synthesized, referred to as a comparative sample Mn_2O_3-2. The third step of MnO_2-to-Mn_2O_3 transformation is performed at an optimal temperature of 600 °C according to the TGA result of precursor $MnCO_3$ (Fig. S3, S4†). Similarly, under air circumstance the thermal decomposition of precursor $MnCO_3$ leads to the formation of porous Mn_2O_3 cubes, defined as another comparative sample Mn_2O_3-3.

Overall and close-up SEM images of precursor $MnCO_3$ show irregular cube-like shapes with an average size of ca. 340 nm (Fig. 1b). At the $KMnO_4$:$MnCO_3$ molar ratio of 1:30, the wet-chemically transformed MnO_2 boxes succeed at the skeleton preservation of $MnCO_3$ cubes, obviously giving a hollow interior and a rough surface (Fig. 1c). Through the high-temperature crystallization and simultaneous release of gaseous O_2, the solid-state transformation of amorphous MnO_2 to cubic Mn_2O_3 endues a hollow porous structure for sample Mn_2O_3-1 (Fig. 1d).

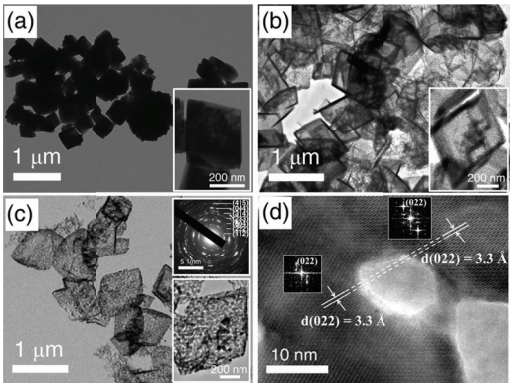

Fig. 2 (a-c) TEM images of precursor $MnCO_3$, intermediate MnO_2 and sample Mn_2O_3-1 in sequence. (d) A representative HR TEM image of the porous shell of a Mn_2O_3-1 box.

TEM images further prove the structural features of low-valence precursors, high-valence intermediates and middle-valence products: cube-shaped $MnCO_3$ (Fig. 2a and an inset), MnO_2 boxes with a thin shell and a big hollow interior (Fig. 2b and an inset) and porous Mn_2O_3 boxes with a thin shell composed of tiny nanoparticles (Fig. 2c, the bottom-right inset). In the upper right corner of panel (c), another inset is the electron diffraction (ED) pattern of cubic Mn_2O_3 with diffraction rings corresponding to the crystal plane (*hkl*)/*d*-spacing (nm) of (415)/0.15, (044)/0.17, (314)/0.18, (233)/0.20, (004)/0.24, (222)/0.27 and (112)/0.38 (Fig. 2c). Fig. 2d is a representative high-resolution TEM image taken by focusing electron beam on the shell of a porous Mn_2O_3-**1** box, showing the integrative lattice fringes of crystal face (022) with an interplanar spacing of ~3.3 Å across the porous gap. Insets in Fig.2d are the corresponding fast Fourier-transformed patterns, indicating a high crystallinity of these porous shells.

When evaluated using a standard Mn_2O_3/Li half-cell model, the 1st discharge profile of Mn_2O_3-1 electrode experiences a monotonic voltage drop from the upper limit of 3 V to a plateau at ~1.3 V then undergoes another voltage drop to a low plateau at ~0.35 V and then sustains a further voltage drop to the lower limit of 0.01 V, giving a specific discharge capacity of 1467 mA h g^{-1} at 800 mA g^{-1} (Fig. 3a). This process can be associated with the stepwise reduction of Mn^{3+} to Mn^{2+} and then to Mn^0, accompanied by the formation of organic polymeric gel-like layer or the so-called solid electrolyte interphase (i.e., SEI) film outside particles' surface. By subtracting the theoretical Li storage capacity of Mn_2O_3 (i.e., 1018 mA h g^{-1}), the residual value of 449 mA h g^{-1} originates from the decomposition of electrolyte or the formation of SEI film. Considering the significant drawback of low conductivity, this working electrode delivers the decreasing discharge capacities of 1125, 580 and 301 mA h g^{-1} in the 2nd, 10th and 50th cycles, respectively (Fig. 3a).

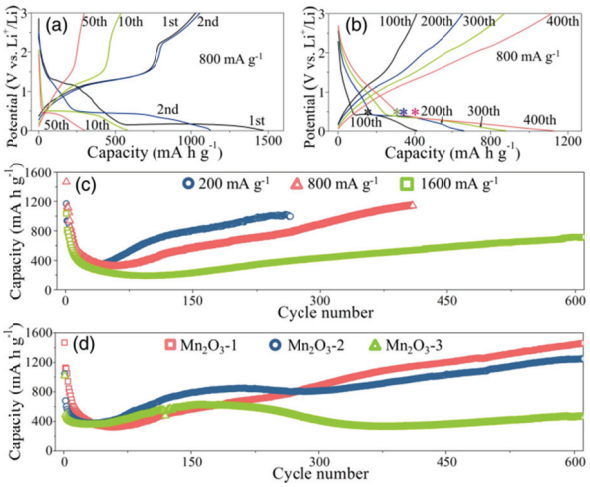

Fig. 3 (a, b) Representative voltage profiles of anode Mn_2O_3-1 operated at 800 mA g^{-1}. (c) Cycling performances of anode Mn_2O_3-1 recorded at different current rates. (d) Electrochemical durabilities of different Mn_2O_3 electrodes conducted at 800 mA g^{-1}.

Over decades of continuous cycles at 800 mA g^{-1}, the capacity loss occurring at each previous-cycle may be overcompensated by an extra contribution of the gradually emerged double-layer capacitance, showing the discharge capacities of 411, 660, 880 and 1127 mA h g^{-1} with the interfacial storage parts of 237, 353, 553 and 718 mA h g^{-1} in the 100th, 200th, 300th and 400th cycles, respectively (Fig. 3b). According to our previous results,[23, 24] after a discharging process the resulting metallic Mn^0 can hardly be converted into manganese oxides completely, which may account for the general capacity loss occurring therein, and then the surface-enhanced storage behavior could emerge from the ordered arrangement of residual metallic Mn^0 accumulated gradually. To the best of our knowledge, so far this surface-enhanced storage phenomenon can only be observed for nanostructured composites composed of nanosized TMOs that were highly dispersed in a layered structure of conductive carbons.[3, 8]

As shown in Fig. 3c, after ~80 cycles these porous Mn_2O_3 boxes (i.e., Mn_2O_3-1 sample) obviously present an upward trend of discharge capacity operated at different current rates. At 200 mA g^{-1} anode Mn_2O_3-1 displays the discharge capacities of 663, 902, 1028 and 1145 mA h g^{-1} with the interfacial storage parts of 291, 510, 692 and 726 mA h g^{-1} in the 100th, 200th, 300th and 400th cycles, respectively; at 1600 mA g^{-1} anode Mn_2O_3-1 displays the discharge capacities of 191, 304, 430 and 529 mA h g^{-1} with the interfacial storage parts of 138, 171, 243 and 302 mA h g^{-1} in the 100th, 200th, 300th and 400th cycles, respectively. Therefore, in the absence of conductive carbons, the so-called surface-enhanced Li storage capability originating from non-faradaic contribution increases with the increasing of cycling numbers.

As mentioned above, another two samples were synthesized and treated as comparisons: seriously agglomerated Mn_2O_3-2 is composed of porous boxes (Fig. S5†) and Mn_2O_3-3 clearly presents a shape of cube with the visually porous feature (Fig. S6†). As shown in Fig. 3d, at 800 mA g^{-1} the initial discharge capacities of Mn_2O_3-1, Mn_2O_3-2 and Mn_2O_3-3 are 1467, 1046 and 1019 mA h g^{-1}

with a retention ratio of 98.2%, 118.6% and 44.5% in the 600th cycle, respectively. Considering both the formation of SEI film at the 1st cycle and the gradual capacity loss during the subsequent ~54 cycles, the overall discharge upward trend of Mn_2O_3-2 can be attributed to the increasing interfacial storage contribution that originates from its structural characteristics similar to those of Mn_2O_3-1 (Fig. 3d, S5†). Aside from the relative big size of building blocks, both the impurity and non-hollow features of Mn_2O_3-3 may answer for the slow penetration of electrolyte and/or the gradual activation of its interior, giving an transient increase of reversible capacity occurring from the 30th to 160th cycle (Fig. 3d, S6†).

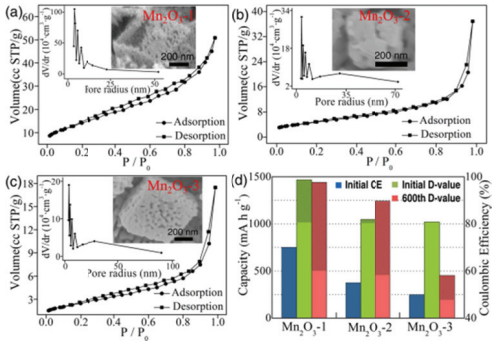

Fig. 4 (a-c) N_2 adsorption-desorption isotherms and the inserted pore size distributions of three porous Mn_2O_3 products. (d) Histograms of the comparative electrochemical parameters of these porous Mn_2O_3 obtained at a current rate of 800 mA g^{-1}.

N_2 adsorption-desorption results of Mn_2O_3-1, Mn_2O_3-2 and Mn_2O_3-3 demonstrate a non-mesoporous nature for all of them and give the BET surface areas of 52.23, 17.63 and 9.23 m^2 g^{-1}, respectively. By comparison, the higher surface area of Mn_2O_3-1 (Fig. 4a) and its achieving interfacial Li storage capability (Fig. 3d) coincide well with both the higher value of initial Coulombic efficiency (i.e., initial CE, Fig. S7†) and the lower values of charge-transfer and surface-film resistances measured at different states (Fig. S8a, b†), whereas these are reverse for the lower surface area of Mn_2O_3-3 (Fig. 4c).[25] Furthermore, the agglomeration of hollow porous Mn_2O_3-2 accounts for both the middle BET surface area and the transient increase of reversible capacity occurring from the 35th to 160th cycle (Fig. 3d, 4b, S9†).

At 800 mA g^{-1} the acquired electrochemical parameters of the three Mn_2O_3 electrodes are summarized for practical application purposes. As shown in Fig. 4d, the higher BET surface area of the sample corresponds to the higher initial discharge capacity (i.e., initial D-value) of the electrode with a higher initial CE, even though all the samples show high CE (>99%) after the first 80 cycles (Fig. S7†). Supposed a complete transformation of Mn^{3+} to Mn^0 in these initial discharges, the initial interfacial contributions of BET surface area can be estimated: 449 (Mn_2O_3-1), 28 (Mn_2O_3-2) and 1 mA h g^{-1} (Mn_2O_3-3) compared to the theoretical value of 1018 mA h g^{-1}, assigned to the adverse effect of SEI film formation (Fig. S8a, b†). As for each parameter of the initial or 600th discharge capacity (i.e., 600th D-value), the fraction of interfacial storage contribution is shaded therein (Fig. 4d). In the 600th cycle, the acquired reversible capacities of Mn_2O_3-1, Mn_2O_3-2 and Mn_2O_3-3 electrodes are 1442, 1241 and 454 mA h g^{-1} with an extra interfacial contribution of 65%, 61% and 59%, respectively. Aside from the large surface area and high electrochemical durability of porous Mn_2O_3-1 boxes (Fig. S10†), after initial 80 cycles the combination of the upward trend of reversible capacity (Fig. 3c) with the increasing plus-value of charge-transfer surface-film resistances (Fig. S8c†) implies the gradual generation of interfacial non-faradaic storage capacity.

In summary, the nanofabrication of a hollow porous Mn_2O_3 nanostructure with the possibly layered arrangement of adjacent shells at nanoscale, composed of single-crystalline building blocks, has been developed using carbonate precursors. The porous Mn_2O_3-1 sample exhibits an upward trend of reversible capacity (e.g., 1442 mA h g^{-1}, the 600th cycle, 800 mA g^{-1}) and can be mainly assigned to the extra interfacial compensation appearing after the initial ~80 cycles. In the absence or presence of conductive carbons, the non-faradaic contribution to an enhanced interfacial Li storage capacity of other hierarchically nanostructured TMOs deserves to be investigated in future.

Notes and references

Key Laboratory for Colloid and Interface Chemistry of Education Ministry, School of Chemistry & Chemical Engineering, Shandong University, Jinan 250100, China. Tel: +86-531-88361387; fax: +86-531-88364464; e-mail: qshen@sdu.edu.cn.

† Electronic Supplementary Information (ESI) available: experimental procedures, further SEM images, XRD, TGA, EIS and charge-discharge results. See DOI: 10.1039/c000000x/

1 Y. Qiu, G.-L. Xu, K. Yan, H. Sun, J. Xiao, S. Yang, S.-G. Sun, L. Jin and H. Deng, *J. Mater. Chem.*, 2011, **21**, 6346.
2 Y. Qiao, Y. Yu, Y. Jin, Y.-B. Guan and G.-H. Chen, *Electrochim. Acta*, 2014, **132**, 323.
3 Y. Sun, X. Hu, W. Luo, F. Xia and Y. Huang, *Adv. Funct. Mater.*, 2013, **23**, 2436.
4 P. Poizot, S. Laruelle, S. Grugeon, L. Dupont and J-M. Tarascon, *Nature*, 2000, **407**, 496.
5 Z. Wang, D. Luan, S. Madhavi, C. M. Li and X. W. Lou, *Chem. Commun.*, 2011, **47**, 8061.
6 J. Maier, *Nat. Mater.*, 2005, **4**, 805.
7 T. Brezesinski, J. Wang, J. Polleux, B. Dunn and S. H. Tolbert, *J. Am. Chem. Soc.*, 2009, **131**, 1802.
8 C. Peng, B. Chen, Y. Qin, S. Yang, C. Li, Y. Zuo, S. Liu and J. Yang., *ACS Nano*, 2012, **6**, 1074.
9 L. Su, Y. Zhong and Z. Zhou, *J. Mater. Chem. A*, 2013, **1**, 15158.
10 S. Chen, Y. Xin, Y. Zhou, Y. Ma, H. Zhou and L. Qi, *Energy Environ. Sci.*, 2014, **7**, 1924.
11 Y. Jiang, D. Zhang, Y. Li, T. Yuan, N. Bahlawane, C. Liang, W. Sun, Y. Lu and M. Yan, *Nano Energy*, 2014, **4**, 23.
12 X. W. Lou, L. A. Archer and Z. Yang, *Adv. Mater.*, 2008, **20**, 3987.
13 J. Liu, H. Xia, L. Lu and D. Xue, *J. Mater. Chem.*, 2010, **20**, 1506.
14 X. W. Lou, D. Deng, J. Y. Lee and L. A. Archer, *Chem. Mater.*, 2008, **20**, 6562.
15 Y. Chen, H. Xia, L. Lu and J. Xue, *J. Mater. Chem.*, 2012, **22**, 5006.
16 Y. Wu, Z. Wen, H. Feng and J. Li, *Small*, 2012, **8**, 858.
17 Y. Zhang, Y. Yan, X. Wang, G. Li, D. Deng, L. Jiang, C. Shu and C. Wang, *Chem. Eur. J.*, 2014, **20**, 1.
18 K.-W. Park, *J. Mater. Chem. A*, 2014, **2**, 4292.
19 H. B. Lin, H. B. Rong, W. Z. Huang, Y. H. Liao, L. D. Xing, M. Q. Xu, X. P. Li and W. S. Li, *J. Mater. Chem. A*, 2014, **2**, 14189.
20 J. W. Ko, J. H. Kim and C. B. Park, *J. Mater. Chem. A*, 2013, **1**, 241.
21 C. Zhao, F. Liu, W. Kang, Y. Su, D. Wang and Q. Shen, *Cryst. Growth. Des.*, 2011, **11**, 2084.
22 J. Fei, Y. Cui, X. Yan, W. Qi, Y. Yang, K. Wang, Q. He and J. Li, *Adv. Mater.*, 2008, **20**, 452.

23 X. Liu, C. Zhao, F. Feng, F. Yu, W. Kang and Q. Shen, *RSC Adv.*, 2015, **5**, 7604.
24 W. Kang, F. Liu, Y. Su, D. Wang and Q. Shen, *CrystEngComm*, 2011, **13**, 4174.
25 L. Li, C. Nan, J. Lu, Q. Peng and Y. Li, *Chem. Commun.*, 2012, **48**, 6945.